

High-Frequency Electromagnetic Purification of Silicon



LUCAS NANA WIREDU DAMOAH and LIFENG ZHANG

The effect of a high-frequency electromagnetic (EM) field on the removal of nonmetallic inclusions from molten silicon was experimentally investigated. Inclusion separation efficiencies of up to 99 pct were reached. The separation efficiency was independent of the particle concentration in the melt and increased significantly with increases in the frequency, separation time, and coil current. Particles were separated from the silicon matrix and relocated to the top, bottom, and side walls of the crucible due to the effect of three mechanisms: induced secondary fluid flow which carried particles from the bulk of the melt; EM body force which worked in the skin-depth area to trap particles on the side wall; and fluid shear force due to the local acceleration of molten silicon, which promoted the settling of particles to the bottom of the crucible and also carried particles toward the top. Higher coil current enhanced the strength of the magnetic field which enhanced fluid flow, while higher frequency also enhanced the fluid acceleration, and the effect of current was more pronounced leading to better particle separation.

DOI: 10.1007/s11663-015-0447-2

© The Minerals, Metals & Materials Society and ASM International 2015

I. INTRODUCTION

RECENT global developments in the energy sector with a drive for the production of clean, reliable, and affordable energy have stirred a rapid growth in the production of photovoltaic (PV) cells.^[1] This has led to growth in silicon-based PV cells which control over 90 pct of the PV market share^[2] either as single-crystalline silicon, or multicrystalline silicon (MC-Si), or amorphous silicon.^[3] MC-Si produced by directional solidification of solar grade silicon melt dominates the silicon PV market.

During the directional solidification process, SiC and Si₃N₄ particles within the molten silicon are pushed by the solidification front to the top of the ingot which is the last to solidify. Therefore, the top of the ingot is cut generating what is known as top-cut solar silicon scrap. The Si₃N₄ particles are mainly from the coating material on the inside surface of the silica crucible and from the air absorption during the solidification process. The SiC particles mainly stem from the carbon reduction process during the primary production of silicon.^[4] For sustainability, the silicon in the top-cut silicon scrap must be recovered. Therefore, methods for removing nonmetallic particles, such as SiC and Si₃N₄, from the silicon are important in order to recycle top-cut silicon scrap to

become a useful feedstock for silicon solar cells manufacturing.

Methods such as sedimentation, filtration, fractional melting, plasma refining, and electromagnetic (EM) separation hold the potential to purify SoG-Si. Although the density of SiC and Si₃N₄ particles are higher than the silicon melt, the sedimentation process poses an industrial implementation challenge since the natural sedimentation requires long periods of time.^[5,6] Fishman^[5,6] reported that during the sedimentation process, natural convection generates a recirculating flow pattern transporting particles to the top and directional solidification pushes the particles into the solidifying liquid at the top. However, these complications might be reduced by performing the sedimentation process in a different furnace than directional solidification. Furthermore, it is also well known that the settling velocity of particles is enhanced in convective melts, except for excessive flow velocities that may result in back diffusion of already settled particles.^[7] Any method that could enhance the particle sedimentation velocity will be advantageous. Filtration using ceramic foam filters to remove SiC and Si₃N₄ inclusions has been investigated by Zhang *et al.*^[4,8] with reported filtration efficiencies of over 97 pct for inclusions >10 μm in size. However, the filtration process also poses certain industrial implementation questions regarding the design of a continuous process, and selection of filter materials that will prevent contamination of the molten silicon. Zhang *et al.*^[8] showed that the filtration process was effective at removing most of the large inclusions but was less effective at removing inclusions smaller than 10 μm which are still very detrimental to the properties of silicon solar cells.

EM removal of nonmetallic particles from silicon has yet to be well explored although it has been studied for inclusion removal from other metals such as aluminum

LUCAS NANA WIREDU DAMOAH, formerly Ph.D. Student with the Department of Materials Science & Engineering, Missouri University of Science and Technology (Missouri S&T), 223 McNutt Hall, Rolla, MO 65409-0340, is now Lecturer with the Department of Materials Science and Engineering, University of Ghana, Legon, Accra, Ghana. LIFENG ZHANG, Dean, is with the School of Metallurgical and Ecological Engineering, University of Science & Technology Beijing, Beijing 100083, China. Contact e-mail: zhanglifeng@ustb.edu.cn

Manuscript submitted June 30, 2015.

Article published online September 21, 2015.

and steel since Kolin,^[9] and later, Leenov and Kolin^[10] proposed the principle. It can introduce magnetic pressure in the melt which has the potential to remove inclusions of all size ranges and could also induce fluid flow that may help to remove particles by settling. Others have applied a gradient magnetic field to the melt to induce magnetization forces that may cause inclusions to rise or settle in the melt.^[11–14] EM separation uses the difference in the electrical conductivity between the inclusions and the melt, and thus, when a uniform EM field is applied to a molten metal, the metal is compressed by the EM force (Lorentz force), and a pressure gradient is generated in the metal. The non-conductive particles or less-conductive particles are forced to move in the opposite direction of EM force, thereby getting separated from the melt.^[15,16] Some feasibility studies on the use of a high-frequency alternating current (AC) EM field to remove suspended particles from silicon has been studied and reported by the authors.^[17–19] The current study investigates the subject further and discusses new experimental results on the effects of processing parameters such as time, coil current, and frequency on the removal of inclusions from silicon under a high-frequency AC EM field. Inclusion separation mechanisms under the AC magnetic field are also presented.

II. MATERIALS AND METHODS

A. Materials

Following the successful trials of this current method of particle separation from silicon with top-cut solar silicon scrap material, and another with a mixture of silicon and SiC particles of different volume fractions, a new Si-SiC composite material with uniform particle dispersion was preferred for parametric investigation. The results of the trial experiments have been published in two international conferences. Top-cut SoG-Si scrap has particles concentrated on one of the sides, and a mixture of solid silicon and SiC particles did not assure uniform particle dispersion. Thus, a uniformly dispersed material was prepared by a “stir-solidification” method in which metallurgical grade silicon and Al-15 pct SiC composite material were melted at 1773.15 K (1500 °C) and continuously stirred until it solidified under argon

gas. The stir-solidification process was undertaken through the following steps:

- Approximately 80 wt pct of metallurgical grade silicon and 20 wt pct Al-15 pct SiC composite material were melted at 1773.15 K (1500 °C) in a fused silica crucible in an induction furnace under an argon gas atmosphere.
- After melting, the furnace was turned off, and the molten material was stirred continuously with a mullite rod until it became solidified.
- The solidified material was allowed to furnace cool to room temperature in the argon gas atmosphere.
- The resulting material was removed from the furnace and sectioned into appropriate sizes to be used in the subsequent particle separation experiments.

Typical microstructures of the materials are shown in Figure 1 to summarize the Si-SiC composite-making process. During cooling after the stir-solidification process, a part of the aluminum (approximately 10 wt pct) precipitated in the eutectic composition with the silicon to the top of the material (see microstructure in Figure 2). This region contained no particles, making the stir-solidification process a good method to produce eutectic Al-Si alloys from metallurgical grade silicon and waste Al-SiC composites, if it ever becomes necessary. The particle-free eutectic composition was separated from the composite materials by removing with the hand or breaking with a hammer where necessary.

The type and size of inclusions in the Si-SiC composite material were determined using an SEM with automated feature analysis capability (ASPEX) as shown in Figure 3. The mean sizes shown are for particles larger than 3 μm . There were, however, a large number of particles smaller than 3 μm which when included in the distribution resulted in an overall average particle size of $5 \pm 5 \mu\text{m}$ with an average area fraction of 11 ± 5 pct particles. The SiO_2 could have resulted from surface oxidation of SiC particles, as the typical EDX composition showed traces of carbon.

B. Equipment and Experimental Set-Up

The experimental equipment is made of a water-cooled copper induction coil of seven turns, 196 mm height, and 150 mm inner diameter. The copper tubing has a 14 mm by 14 mm square cross section and 12-mm

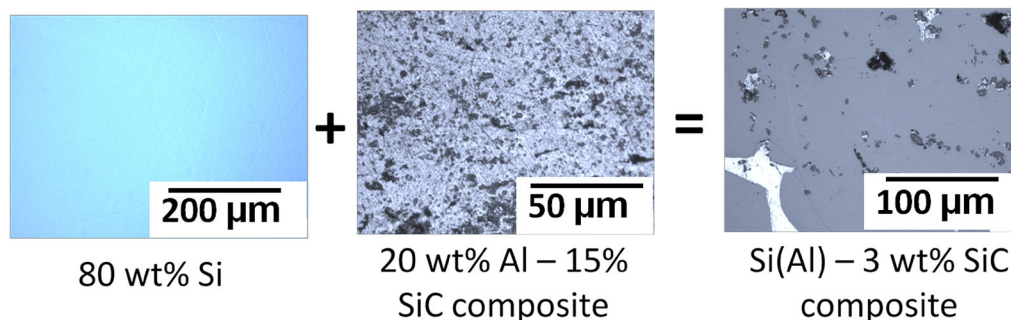


Fig. 1—Microstructure of Si(Al)-3 pct SiC composite material made from metallurgical silicon and Al-15 pct SiC composite through the stir-solidification process.

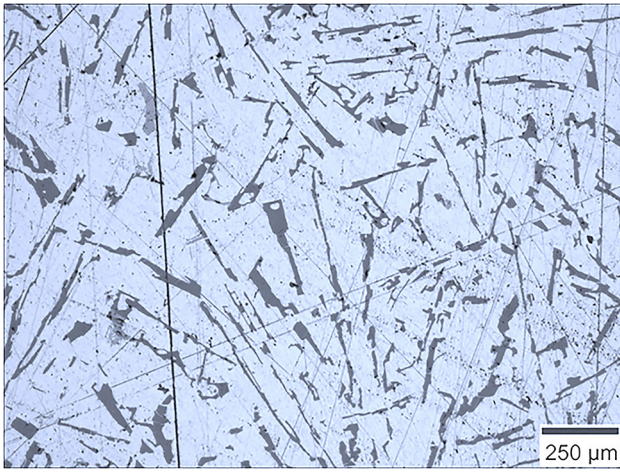


Fig. 2—Typical microstructure of the aluminum dominant Al-Si eutectic structure of the material that precipitated on top of the solidified Si(Al)-SiC composite material during the stir-solidification process.

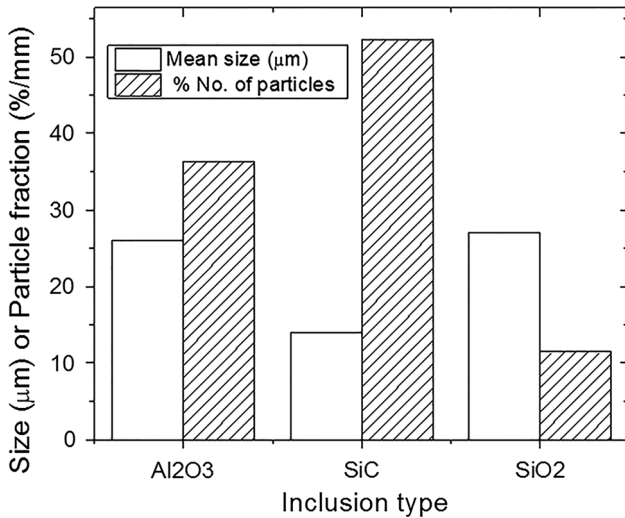


Fig. 3—Type and average size of inclusions in the Si-SiC composite material.

adjacent turn spacing. The coil was powered by a 100-kW generator with a capacitor bank and the capability to change frequency within the range of 50 to 200 kHz by changing the capacitance within the circuit. The power supply is also equipped with a LCD touch screen panel where power input can be made, and the current, voltage, frequency, and power information were recorded during the experiment. The set-up included a graphite susceptor and a crucible. Figure 4 shows a picture of the experimental equipment, and Figure 5 shows the schematics of the experimental set-up.

C. Experimental Procedure

The Si(Al)-SiC composite material prepared by the stir-solidification process was cut into pieces of approximately 54 g mean size for this study. Table I

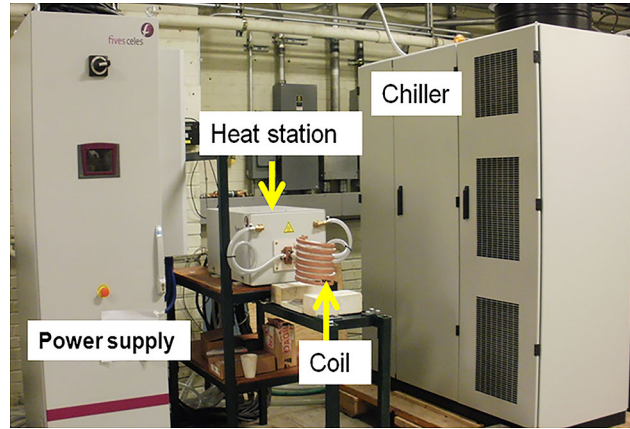
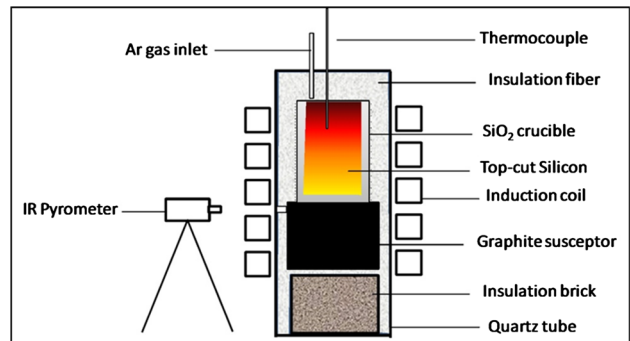
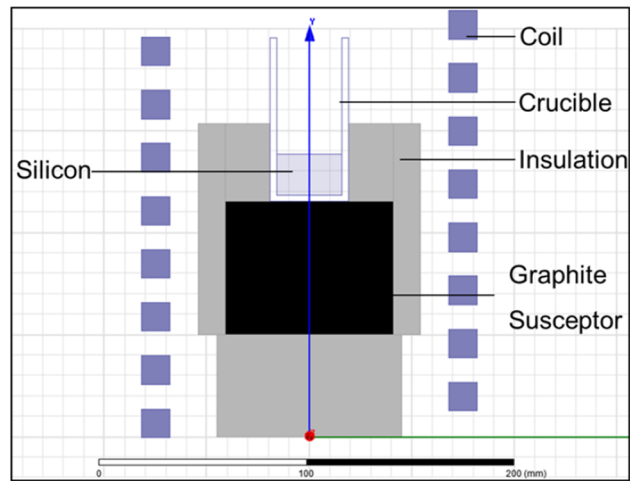


Fig. 4—Picture of the equipment showing the coil-power supply system.



(a)



(b)

Fig. 5—Schematic of the experimental set-up for the electromagnetic separation of particles from silicon (a) complete set-up and (b) scaled schematic of relevant components.

summarizes the experimental plan used in this study. The experiment followed three main steps:

- **Melting** The composite material was placed in the crucible set in place within the coil. The power supply was turned on and the sample monitored until melting. The melting duration predetermined after a series

Table I. Experimental Plan and Actual Separation Parameters

Exp. #	Material Si(Al)-SiC (g)	Capacitance, C (#) and μF	Parameters				Separation Time (s)	Coil Current, (A) $I_{\text{rms}} = 2\pi fCV$
			I (A)	V (V)	f (kHz)	P (kW)		
C10-1	56.0468	(4) 2.64	17.6	262	64	4.3	10	278
C10-2	53.6120	(4) 2.64	21.5	312	64	6.0	10	331
C10-3	64.1534	(4) 2.64	31.5	499	65	13.6	10	538
C10-4	59.2054	(4) 2.64	42.4	502	65.5	18.4	10	545
C25-1	53.4226	(4) 2.64	17.5	264	64	4.35	25	280
C25-2	56.1613	(4) 2.64	22	308	64.5	6.15	25	330
C25-3	58.7110	(4) 2.64	32	492	64	13.6	25	522
C25-4	59.2617	(4) 2.64	44.3	502	65.5	19.0	25	545
C45-1	56.3080	(4) 2.64	17.7	261.5	64	4.35	45	278
C45-2	55.6334	(4) 2.64	22.3	305	65	6.2	45	329
C45-3	55.8530	(4) 2.64	35.9	454	65	14.2	45	490
C45-4	59.5975	(4) 2.64	41	502	65.5	18.1	45	545
C60-1	56.0378	(4) 2.64	19	259	65	4.5	60	279
C90 -1	54.6405	(4) 2.64	20	260	64.5	4.5	90	278
C120-1	58.9530	(4) 2.64	18.2	260	64	4.4	120	276
C45-1/4	59.4218	(4) 2.64	17	253	64	4.1	45	269
D10-1	43.9048	(3) 1.98	16.2	301	74	4.6	10	277
D25-1	56.2552	(3) 1.98	16.6	300	74	4.7	25	276
D45-1	59.3491	(3) 1.98	16.8	298	74	4.7	45	274
E10-1	41.5848	(2) 1.32	15.6	371	89	5.5	10	274
E25-1	42.6131	(2) 1.32	16	370	89	5.5	25	273
E45-1	44.4584	(2) 1.32	16.4	374	90	5.6	45	279
CB1	120	(4) 2.64	20	325	65	5.9	90	350
CB2	120	(4) 2.64	19.8	326	64	5.9	30	346
CB3	120	(4) 2.64	20	318	64	5.9	30	338

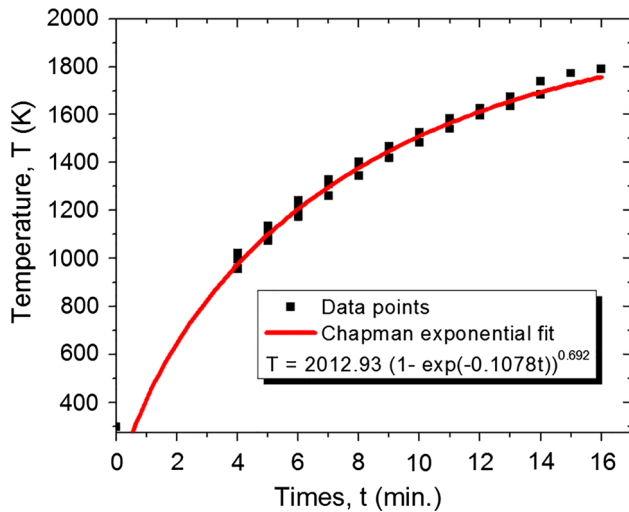


Fig. 6—Heating rates recorded for the experiments.

of trials was set at 16 minutes at a coil current of 230A before particle separation. Hence, all samples were melted under the same coil current for 16 minutes before separation. The heating process followed the rate described in Figure 6. The temperature was measured by means of a calibrated infrared pyrometer which was positioned 1 m away from the coil. After the melting time elapsed, the power supply was turned off.

- *Particle separation* The separation conditions of frequency and coil current were set immediately after

turning off the power supply following sample melting. The power supply was turned on again and the duration of separation recorded with a stop watch. When the desired separation time was attained, the power supply was switched off.

- *Still air cooling* After particle separation, the sample was cooled to ambient temperature in still air.

The cooled sample was then sectioned vertically to form four quarter sections as illustrated in Figure 7. A quarter vertical cross-sectional sample was polished for each experiment and analyzed by means of optical macro- and microscopes and SEM/EDX.

D. Evaluation of Separation Efficiency, η

The particle removal efficiency for a melt with an initial particle concentration C_o and a final concentration C can be defined as follows:

$$\eta = \frac{C_o - C}{C_o} \times 100 \text{ pct} = \left(1 - \frac{C}{C_o}\right) \times 100 \text{ pct} \quad [1]$$

Takahashi and Taniguchi^[15] presented a mass balance of inclusions within the melt which could be adopted and modified as

$$-V \frac{dC}{dt} = (A_W u_W + A_B (u_B + u_t) + A_T u_T) C = aC, \quad [2]$$

where V is volume of melt; A and u are the surface area of separator and particle velocity, respectively; and “ a ” is a certain constant. The subscripts W, B, t, and T represent respectively, the side wall, bottom,

terminal, and top. Equation [2] could be solved with the initial condition $C = C_o$ when $t = 0$ s and substituted into Eq. [1] as follows.

$$\ln(C) - \ln(C_o) = -\frac{a}{V}t = -\lambda t \quad [3]$$

$$\frac{C}{C_o} = e^{(-\lambda t)} \quad [4]$$

$$\eta = (1 - e^{(-\lambda t)}) \times 100 \text{ pct}, \quad [5]$$

where λ is a constant for the separation process that relates the magnetic field and flow parameters. Equation [5] indicates an exponential dependence of the separation on time and other parameters, such as volume of melt and particle velocity, which depend on the magnetic field strength, current density, and frequency.

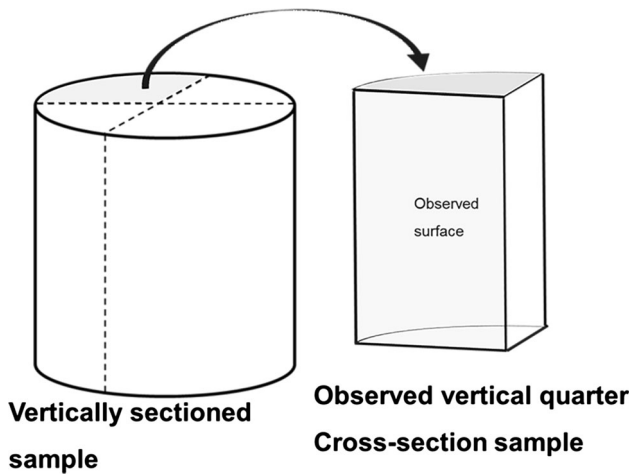


Fig. 7—Sample sectioning and observed surface. Sample is aligned with gravity direction from top to bottom.

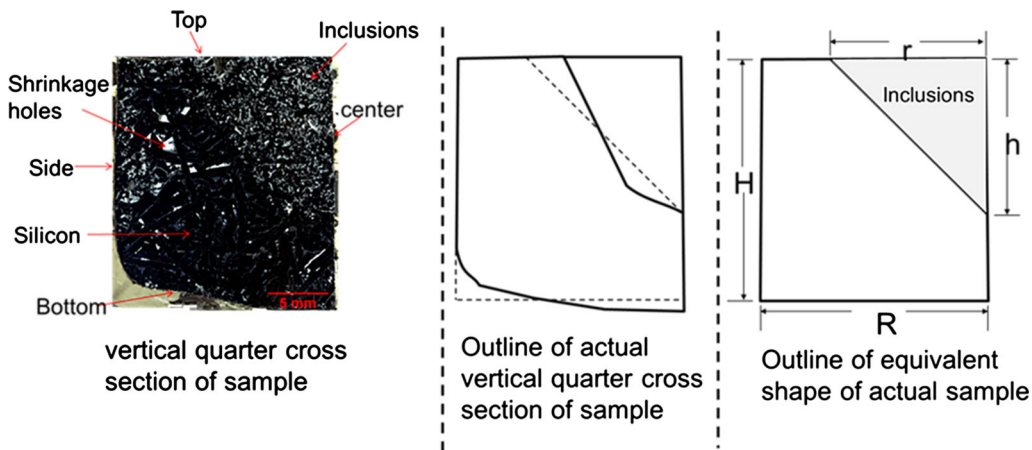


Fig. 8—Vertical cross section of an actual sample with an outline and equivalent shape, and dimensions of the sample architecture with a shaded region of inclusion.

The separation efficiency for the experiments was measured as the ratio of the volume of effective separation regions to the total volume of the sample. The effective separation regions were taken as the region where the matrix is clean with no inclusions in addition to the separated regions with particles at the side and bottom of the sample. This is based on the assumption that particles have accumulated at the side and bottom walls due to the confinement or restrictions imposed by the walls. Figure 8 shows an example of an optical macrograph of the quarter vertical cross section of a separated sample and the outline of equivalent shape of the sample architecture in which the area of the sample occupied by inclusions is shaded.

It must be noted that the experimental sample taken is based on the assumption of 3D symmetry. In 3D, the equivalent outline of the sample is a quarter cross section of a cylinder and the region of inclusions represents a cone. The separation efficiency (η), which is volume fraction of the clean region, was defined as the ratio of the difference between the volumes of the equivalent cylinder and cone to the volume of the equivalent cylinder, expressed quantitatively as:

$$\eta = \frac{(\pi R^2 H) - (\pi r^2 h/3)}{(\pi R^2 H)} = 1 - \frac{h}{3H} \left(\frac{r}{R}\right)^2. \quad [6]$$

According to Eq. [5], the separation efficiency has exponential dependence of time with a pre-exponential parameter of unity. However, when the separation efficiency–time plot from the experiment was fitted with the model, a non-unity pre-exponential parameter was recorded as shown for example in Figure 9(a). This means that before the separation process was timed, some particles had already separated. Therefore, the actual separation time had to be determined by means of the fitted equation, and then a corrected plot made as shown in Figure 9(b). The adjustment corresponded to an average pre-separation time t_o of 90 ± 10 seconds for the experiments.

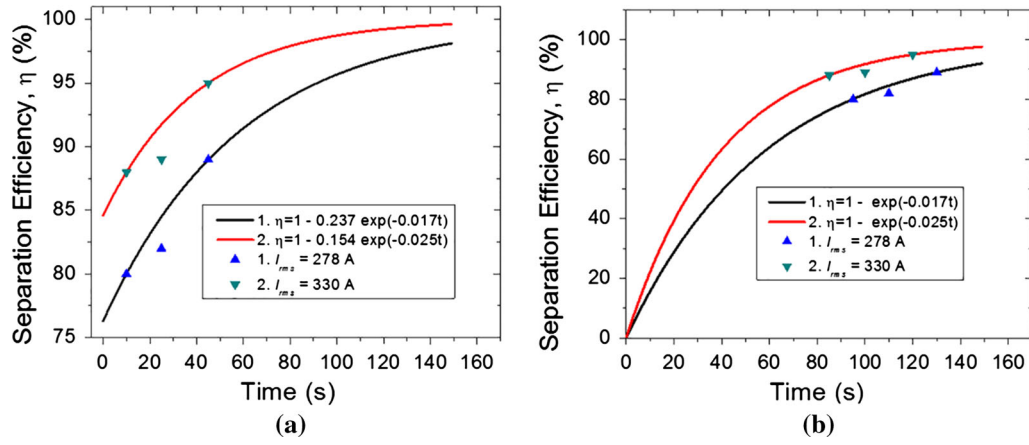


Fig. 9—Example of separation efficiency—time plot (a) based on experimental duration and (b) based on corrected time taken into account pre-separation during the melting process.

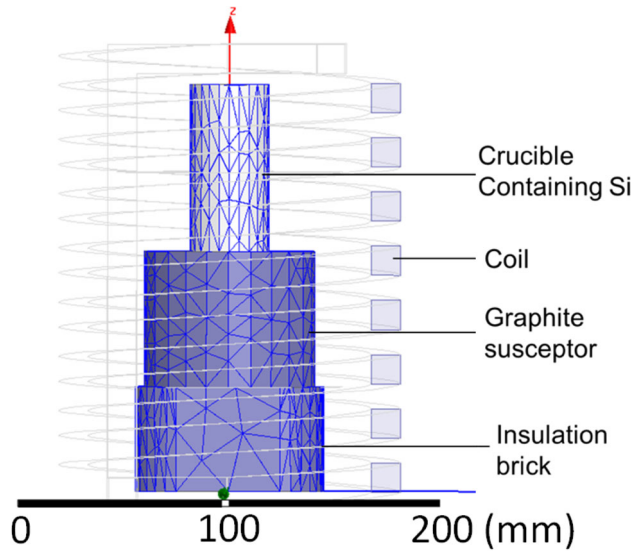


Fig. 10—View of the skin-depth-based mesh of the 3D geometry of solids within the coil.

E. Modeling of Magnetic Field and Fluid Flow

To understand the particle separation mechanism, magnetic field and fluid flow simulations were undertaken. The magnetic field in the experimental set-up was modeled in the finite element magnetic field simulation software ANSOFT Maxwell, and the MagnetoHydroDynamics (MHD) was calculated *via* ANSYS Fluent utilizing the magnetic field data from the ANSOFT Maxwell calculations.

1. Modeling of magnetic field

A 3D model of the experimental set-up was created to scale in ANSOFT Maxwell, and the eddy current solver was used to simulate the EM field which is described by Maxwell's equations (Eq. [7]):

$$\begin{cases} \nabla \cdot B = 0 \\ \nabla \times E = -\frac{\partial B}{\partial t} \\ \nabla \cdot D = q \\ \nabla \times H = j + \frac{\partial j}{\partial t} \end{cases}, \quad [7]$$

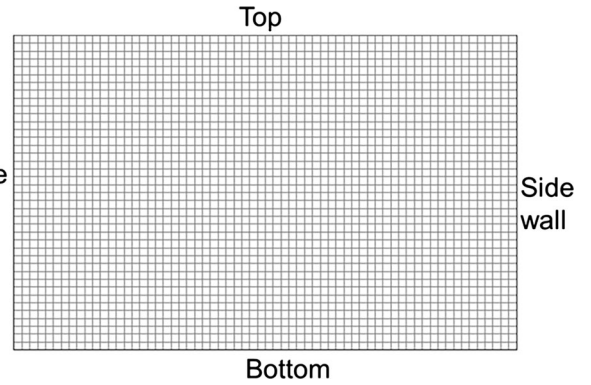


Fig. 11—2D Mesh of the model solved in ANSYS Fluent.

where B (Tesla) and E (V/m) are the magnetic and electric fields, respectively; and H and D are the induction fields for the magnetic and electric fields, respectively. q (C/m³) is the electric charge density, and j (A/m²) is the electric current density vector. The skin-depth-based approach was adopted to mesh the model shown in Figure 10, and the insulation boundary condition was employed in the calculation. This boundary condition assumes there is a perfectly insulating sheet between electrical conductors and that current cannot cross it, and the magnetic field is tangential to the boundary.

2. MHD modeling with ANSYS Fluent

A 2D model of the experimental case was created and meshed in ANSYS Gambit for a cylindrical crucible of 32 mm diameter by 20 mm height. The mesh was made up of 2560 quadrilateral cells of 0.5 mm × 0.5 mm and 2665 nodes. Figure 11 shows the structure of the mesh.

Ohm's law and Maxwell's equations present the coupling between the EM and fluid velocity fields. Equation [8] defines Ohm's law for an electrically conductive molten metal with a velocity field U :

$$j = \sigma(E + U \times B) \quad [8]$$

The magnetic induction equation can be derived from Eqs. [7] and [8] for a conductive medium as

Table II. Data of Materials Properties Used in the Calculations

Property	Silicon	SiO ₂ crucible	Graphite
Density, ρ (kg/m ³)	2570	2210	/
Viscosity, η (kg/m s)	0.000543	/	/
Thermal conductivity, k (W/m K)	58	2.01	/
Specific heat capacity, C_p (j/kg K)	900	733	/
Electrical conductivity, σ (S/m)	1,400,000	0	1,200,000
Magnetic permeability, μ (H/m)	1.26×10^{-6}	1.26×10^{-6}	1.26×10^{-6}

$$\frac{\partial b}{\partial t} + (U \cdot \nabla)b = \frac{1}{\mu\sigma} \nabla^2 b + ((B_0 + b) \cdot \nabla)U - (U \cdot \nabla)B_0 \quad [9]$$

where B_0 and b are the externally imposed and induced magnetic fields, respectively; and μ and σ are the magnetic permeability and electrical conductivity of the molten metal, respectively. And the current density based on Ampere's law is given by

$$j = \frac{1}{\mu} \nabla \times (B_0 + b) \quad [10]$$

The boundary condition for the induced field was set as electrically insulating which means $j = 0$, and the tangential components of the magnetic field are zero.

2D transient turbulent fluid flow and heat transfer for the model were calculated by solving the continuity equation, two Navier–Stokes momentum equations, the two equations for turbulent energy and its dissipation rate, and the general energy equation. Due to the effects of the EM fields, additional source terms are introduced to the fluid momentum equation (*i.e.*, Lorentz force (N/m³) given by Eq. [11]) and the energy equation (*i.e.*, Joule heating rate (W/m³)) given by Eq. [12]

$$F = j \times B \quad [11]$$

$$Q = \frac{1}{\sigma} j \cdot j \quad [12]$$

The no-slip and stationary-wall boundary conditions were employed for the momentum equations. The temperature boundary conditions used are 1823.15 K (1600 °C) for the side wall, 1973.15 K (1700 °C) for the bottom wall, and a backflow temperature of 1773.15 K (1500 °C) same as the temperature of molten silicon. The wall thicknesses were 0.003 m for both the side and bottom walls. Table II presents data for materials properties used in the calculations. For the initial conditions, the velocity and turbulent parameters were all set to zero. The solution was obtained by iterating at a time step-size of 1.0×10^{-5} seconds to account for the possible high-frequency errors.

III. RESULTS AND DISCUSSION

A. Overall Separation

For a complete view of the quarter vertical cross-sectional sample taken for the various experiments to

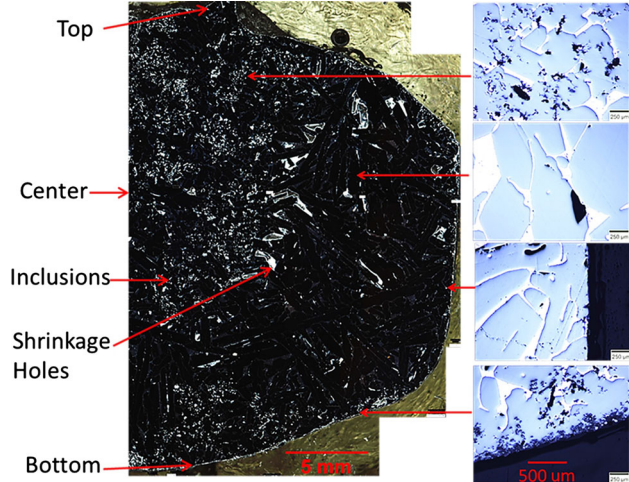


Fig. 12—Typical optical macro- and micrographs of the quarter vertical cross section of the EM-separated sample.

understand the separation process, combined optical macrographs were acquired. In general, particles accumulate at the side wall, bottom wall, and close to the center at the top of the sample. The particles first moved to the central part at the top, and then started settling through the central region of the sample toward the bottom. The optical macrograph shown in Figure 12 indicates the separation of particles from portions of the sample close to the wall and the bottom, leaving a cleaner matrix at these regions.

The microstructures of the various regions in the macrograph are also shown in the figure. The dark phase is the primary silicon phase, the gray phases within the primary silicon is the aluminum-dominant Al-Si eutectic phase, and the bright spots are the nonmetallic particles. Many areas of porosity can be observed in the sample as a result of solidification shrinkage. Between the liquidus and solidus temperatures of the system, the primary silicon (~92 wt pct Si) solidified first and contained the Al-Si liquid at the grain boundaries, which was forced to the top due to pressure from grain growth leaving voids within the grains. Comparing the micrographs of the side wall with the bottom wall, a thinner layer of particles was observed at the side wall than at the bottom of the crucible. The particles observed within the central part of the sample were dispersed and clustered. These particles appeared to have been acted upon by a certain downward pressure causing what seems like particle settling with difference velocities from the top close to the central part and also close to the bottom. Figure 13 shows SEM micrographs

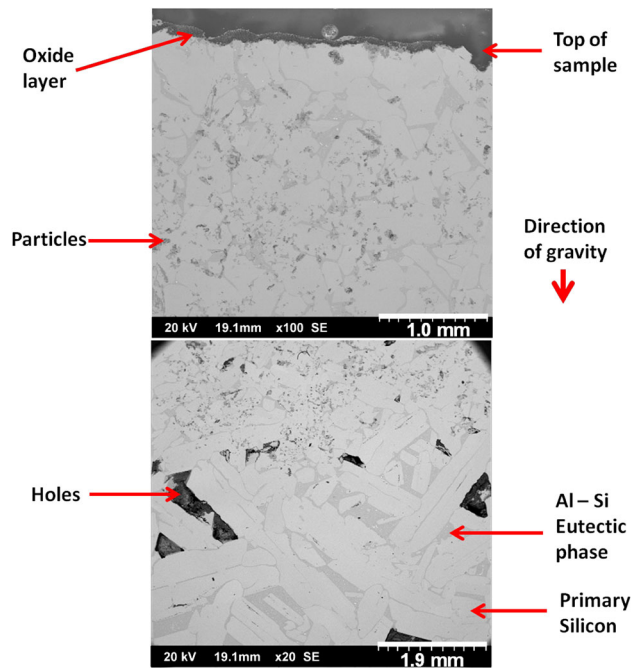


Fig. 13—SEM micrographs of the top part of the samples in Fig. 12 after separation showing a thin topmost oxide layer of aluminum and silicon oxide and the transition from the particles in the top area to the clean area. Many areas of porosity are also observed.

of the top part of the sample. A thin layer of particles can be observed at the top beneath the epoxy-mounting material (dark layer). This particle was determined by EDX to contain mainly Al, O, and Si. This layer is attributed to the atmospheric oxidation of the melt.

Figure 14 shows the distribution of particles at the bottom, side wall, and center of the crucible. In general, the central part of the sample was clean and particles were not detected. On the other hand, thick and dense particle layers were observed near the side wall and the bottom of the samples. An interesting observation is the size and locations of the trapped particles in the layers at the side wall and the bottom of the samples. It can be seen that larger particles were trapped closest to the walls, while fine particles accumulated and deposited on the large particles. This confirms the idea that large particles are easier to separate than smaller particles. Smaller particles are easily carried by the motion of the fluid, and therefore, they have longer residence time within the fluid flow before being separated. A typical EDX area spectrum of these small particles is shown in Figure 15, which shows that the major elements are Si, Al and O. This indicates that some of the original particles might have been oxidized during the experiments. The original sample did not contain Al_2O_3 particles smaller than $5 \mu\text{m}$, unlike the SiC particles over 50 pct of which were smaller than $3 \mu\text{m}$.

The observation of the texture of the particle layer at the bottom and side walls (see Figures 12 and 14) suggests the presence of strong downward and side forces confined to a certain distance from the bottom and side of the crucible, respectively. The particle layer at the bottom was dense and appeared cemented. A similar observation was

made for the particle layer at the side wall, but it was much thinner than the bottom layer.

The downward force is attributed to the contribution of the EM-induced flow in the molten silicon coupled with gravity and fluid shear forces. Fluid shear forces result due to the development of local acceleration due to the unsteady nature of the EM field. These forces increased the particle settling rate and, therefore, causes particles being carried by the flow eddies to have a net downward motion. Due to uneven distribution of fluid velocity throughout the sample (as will be shown in the next section), particles that appear to be settling in the center also settle at different rates. Particles closer to the bottom have higher settling velocities due to the stronger flow in these regions.

The magnetic field distribution vectors within the experimental set-up and contours within the molten silicon for various currents and frequencies calculated via the ANSOFT Maxwell simulations are showed in Figure 16. The strength of the magnetic field increases strongly with the increasing current and slightly with increasing frequency. Within the molten silicon, the magnetic field is concentrated within a layer close to the side wall and diffuses until it reaches a minimum value at the center. The high intensity of the magnetic field near the surface of the molten silicon is due to the limiting effect of skin depth at high frequencies. The skin depth (δ) which depends on the electrical conductivity (σ) of the molten metal, and the frequency is defined as:

$$\delta = \frac{1}{\sqrt{\pi\mu\sigma f}}, \quad [13]$$

where μ is the magnetic permeability of the conductor.

Therefore, the EM body force acting on the particles is the most effective in the vicinity of the side wall. The EM-induced circulatory flow carries particles throughout the fluid, and when these particles are in the vicinity of the walls where settling and EM forces are effective, they are trapped. The remaining particles are carried with the flow and deposited at favorable sites where the fluid flow is weak.

B. Separation Mechanisms and Fluid Flow

1. Contributing forces

From the foregoing discussion, three important phenomena contributed to the separation process:

- EM body force (EM particle force).
- effect of fluid flow.
- effect of fluid shear force.

The forces acting on the particles within the molten silicon may be classified as body, surface, and collision forces. By the Lagrangian particle translational equation of motion, the rate of change of the linear momentum of a particle of mass m_p and moving with a velocity U_p may then be expressed as the sum of the various forces, as expressed by Eq. [14]

$$F_p = m_p \frac{dU_p}{dt} = F_{\text{body}} + F_{\text{surface}} + F_{\text{collision}}, \quad [14]$$

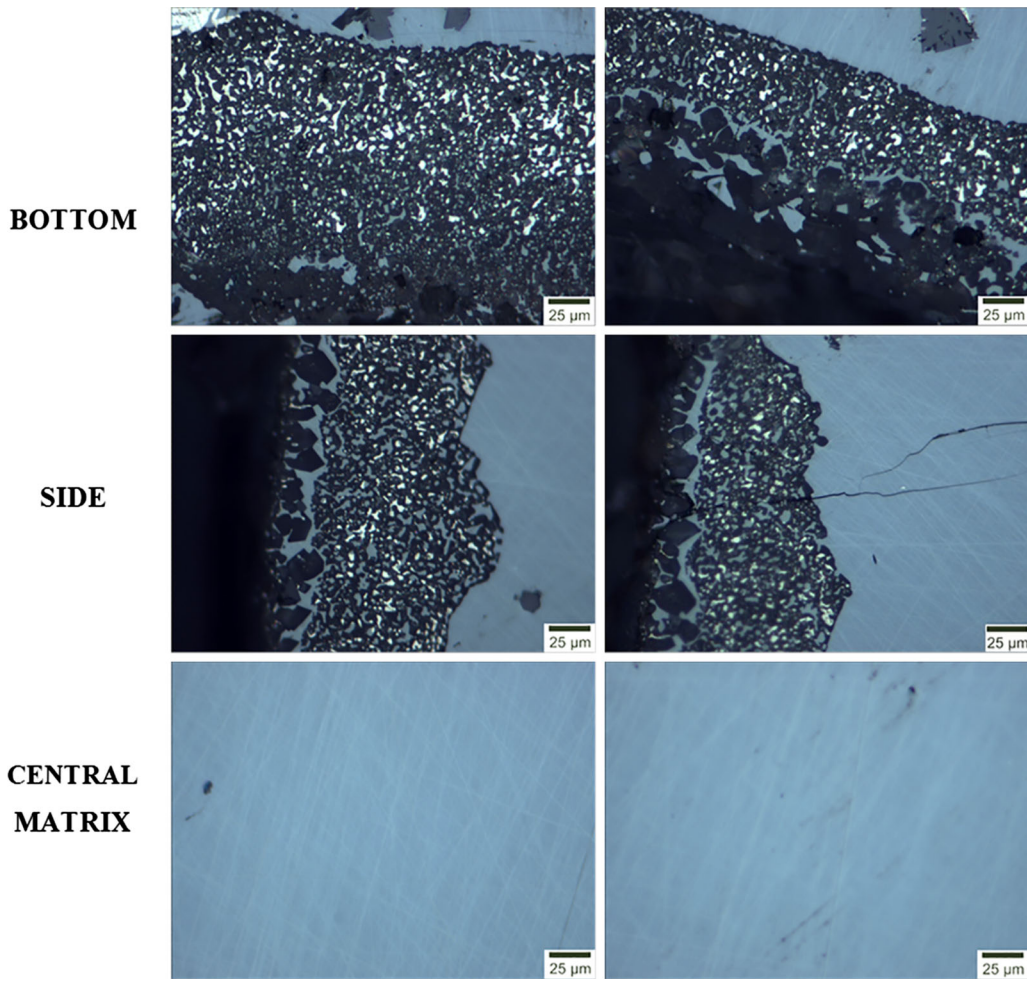


Fig. 14—Micrographs of the various locations capturing the distribution of particles at bottom (top), side wall (middle) and center (bottom) for separation at frequency of 65 kHz, coil current of 533 A and a time of 10 s.

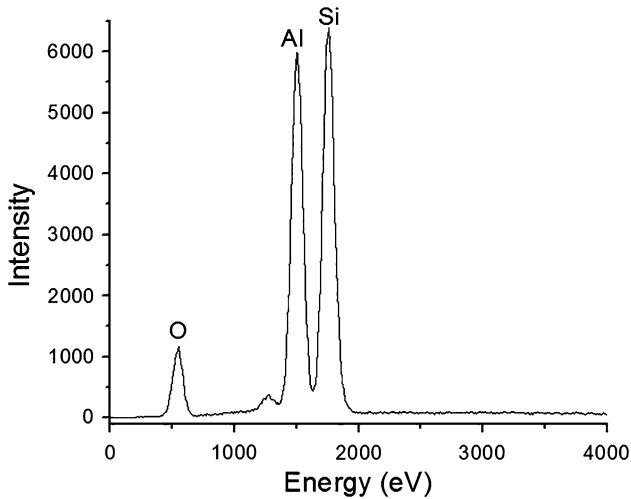


Fig. 15—Typical EDX spectrum of the small size particles in the side and bottom wall layers.

where F_p is the net force acting on the particle. Considering a single particle at a location within the molten metal, and neglecting collision, magnetization, lift, virtual mass,

history, Brownian and thermophoretic forces, the surface and body forces reduce, respectively to Eqs. [15] and [16], and the particle force balance becomes Eq. [17]

$$F_{\text{body}} = F_g + F_B, \quad [15]$$

$$F_{\text{surface}} = F_D + F_S, \quad [16]$$

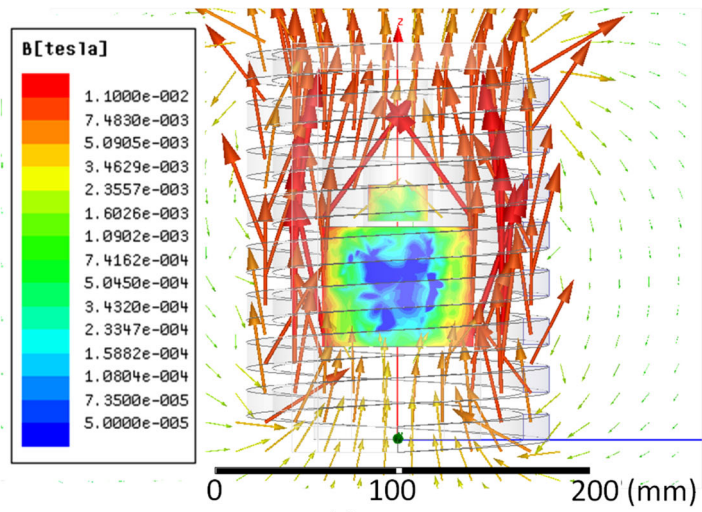
$$F_p = F_D + F_g + F_B + F_S \quad [17]$$

where

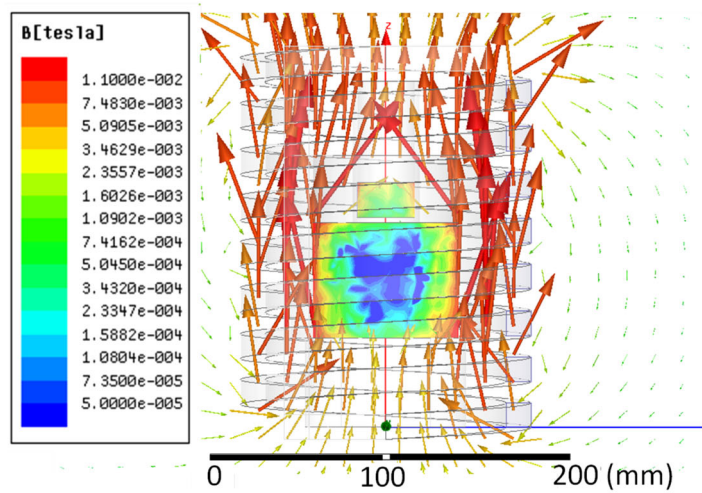
$$\text{Buoyancy force : } F_g = V_p(\rho_p - \rho_f)g \quad [18]$$

$$\text{Electromagnetic body force: } F_B = -\frac{3}{4}V_p(J \times B) \quad [19]$$

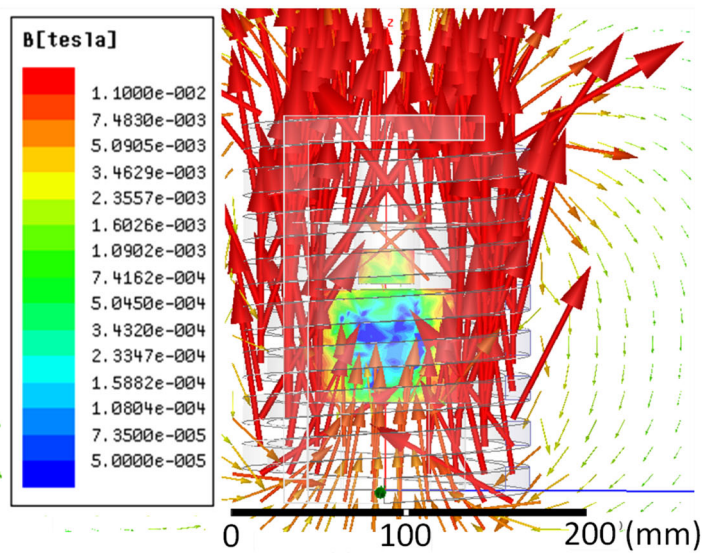
$$\text{Drag force : } F_D = -\frac{1}{8}\pi d_p^2 C_D(U_f - U_p) \quad [20]$$



(a)



(b)



(c)

Fig. 16—Magnetic field vectors within the experimental set-up and B contours within the crucible, sheath, susceptor and silicon for (a) 280 A, 65 kHz, (b) 280 A, 90 kHz, and (c) 535 A, 65 kHz.

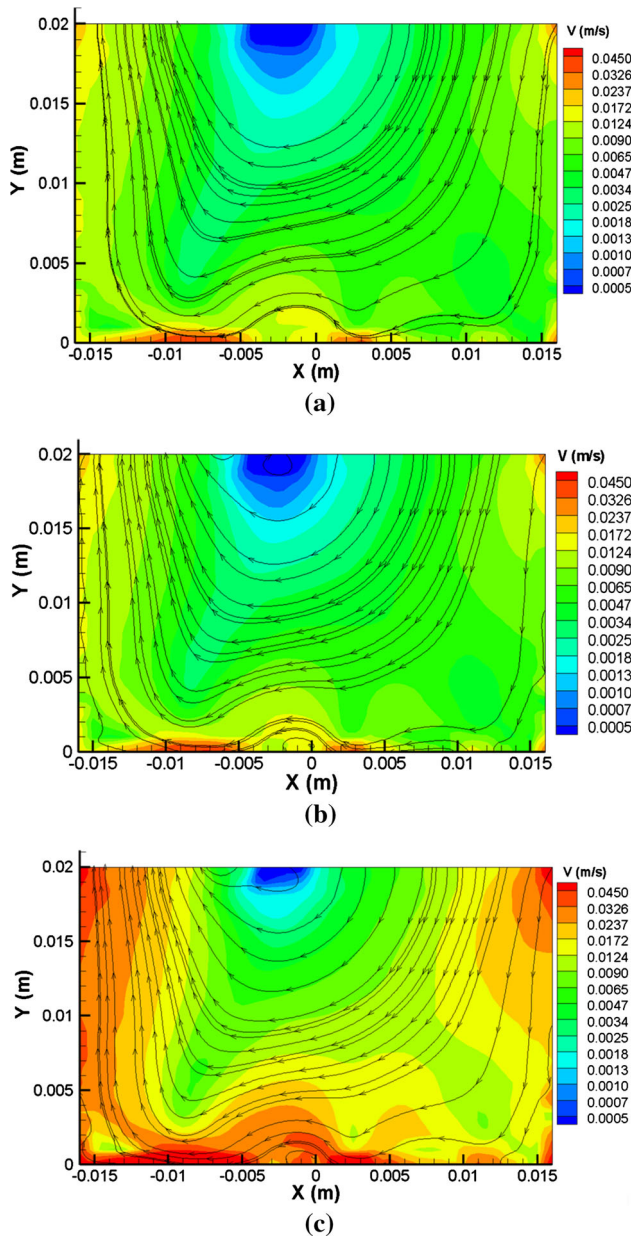


Fig. 17—Contours of velocity magnitude and streamlines of fluid flow as calculated by ANSYS Fluent for (a) 280 A, 65 kHz, (b) 280 A, 90 kHz, and (c) 535 A, 65 kHz.

$$\text{Fluid shear force : } F_S = \rho_f V_p \left(\frac{DU_f}{Dt} \right)_p, \quad [21]$$

where d_p is the particle diameter, V_p is the volume of particle, ρ_p is the density of particle, ρ_f is the density of liquid silicon, $J \times B$ is the Lorentz force, C_D is the drag coefficient, U_f is the velocity of molten silicon, U_p is the velocity of particle.

The fluid shear force arises as a result of local acceleration of the molten silicon around a particle due to the unsteady nature of the EM field. The fluid acceleration, evaluated at the location of the particle, is proportional to the local velocity of the fluid, and the

proportionality constant is proposed as the frequency (f) of the EM field. This is because the rate of change of the magnetic field will control the rate of change of the local fluid velocity. Thus,

$$\left(\frac{DU_f}{Dt} \right)_p = f \cdot (U_f)_p \quad [22]$$

Examination of the Eqs. [18] through [22] suggests that toward the center of the fluid outside of the skin-depth area since the magnetic field is weak, the fluid shear stress will be the dominant force influencing particle motion. It is thus believed that the fluid shear force is responsible for the settling of particles.

The EM body force is the force which acts on the nonconductive particles in a direction opposite to the Lorentz force. It is 3/4 of the magnitude of the Lorentz force and is concentrated within the skin depth of the alternating magnetic field.

The settling force had contributions from the induced fluid flow and fluid shear force. Many researchers in diverse fields have studied the effect of flow on the settling behavior of particles in fluids and have concluded that particles settle faster in more convective fluids.^[20–22] One proposed mechanism for this result is that particles interact with the underlying turbulence and concentrate preferentially in certain flow regions, leading to particle clustering and increases in characteristic size^[22] leading to an enhanced settling. Another possible reason is a decreased fluid viscosity leading to lowering of the resistant forces in the molten metal, thereby enhancing particle settling velocity. It is important to emphasize at this point that, if the convective forces are too strong, particles may be carried in the flow instead of settling, and already settled particles may be eroded. This effect could also lead to the agglomeration of small particles into larger ones, which in turn could enhance their settling rates.

2. Fluid flow

When the EM field is applied to the molten metal, the magnetic field (B) and current density (J) fields combine to create the EM force known as the Lorentz force (given by JB) at orthogonal angles to each other. Strong flow is induced as a result of Lorentz force acting on the molten silicon. Figure 17 shows the flow pattern in the molten silicon calculated by ANSYS Fluent for various currents and frequencies of a vertical plane through the center of the crucible. The streamlines show that fluid flow develops mainly from the top and bottom and drives the molten silicon in a circularly flow pattern. The strongest flow is recorded near the bottom of the molten metal and part of the side walls. Figure 18 presents numbers for the molten silicon velocity statistics for various parameters. Comparisons between various parameters indicate that the fluid velocity is enhanced by increasing both the frequency and current of the magnetic field. However, higher current has a stronger effect on the velocity than higher frequency.

The calculated flow pattern could explain the observed particle distribution in the experiments. In the experiments, particles were trapped at the wall due

to EM forces, others settled due to the effect of fluid shear forces, and yet others carried by the flow were deposited at the top central region. It can be seen from the flow pattern that, the top central region has the least flow, and therefore, offers the most stable place for inclusions circulation within the fluid flow. These particles that circulate in the flow near the central region may agglomerate due to local attractive forces, enhanced by collision *via* fluid or convective transport to become larger and more stable to settle through the fluid. It should also be noted that, along the height of the molten silicon, the flow is nonuniform, and therefore, particles at different locations along the height will settle at different rates, which explains the observed experimental results of apparent different settling velocities of particles through the central part of the melt. Therefore, in a fluid with a more uniform and strong

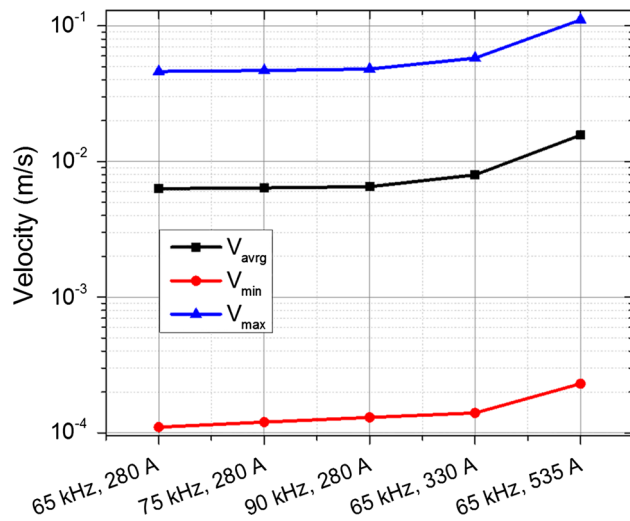


Fig. 18—Comparison of faceted minimum, maximum, and average fluid velocities for various parameters.

fluid velocity field, all particles could be settled. This idea was verified by using a graphite sheath around the crucible with the aim of shielding the strongest part of the magnetic field and inducing a more uniform field within the melt to cause a more uniform flow for settling particle. The result of this study, which is the subject of another article, showed good agreement with the idea. Interestingly, magnetic field calculations showed a much stronger induced field for this case, leading to stronger fluid flow, and hence effective settling of particles.

C. Effect of Separation Time

As expressed by Eq. [5], increasing the separation time should significantly improve the separation process. The results shown in Figure 19 indicate an improved separation for longer separation times. However, due to the settling effect on the particles by the various forces, particles congregated close to the top of the sample by convective forces and settled through the melt over time, and could lead to clusters of particles being observed within the matrix for incomplete settling. Similar observation of this phenomenon was made for other separation conditions of currents and frequencies (see Figure 20 at 90 kHz for example). It is important to note that during the experiments, separation time started after the melt had been under the magnetic field for a while (*i.e.*, t_o), and therefore, the times reported in the figures are the recorded experiment duration, which is explained in Section II–D, could be adjusted based on an exponential fit (Eq. [6]).

D. Effect of Coil Current, I_{rms}

Increasing the coil current increases the strength of the magnetic field and increases the separation efficiency of the process. A stronger magnetic field produces stronger forces and stronger fluid flow (as seen in Section III–B) which leads to better separation. However, due to the

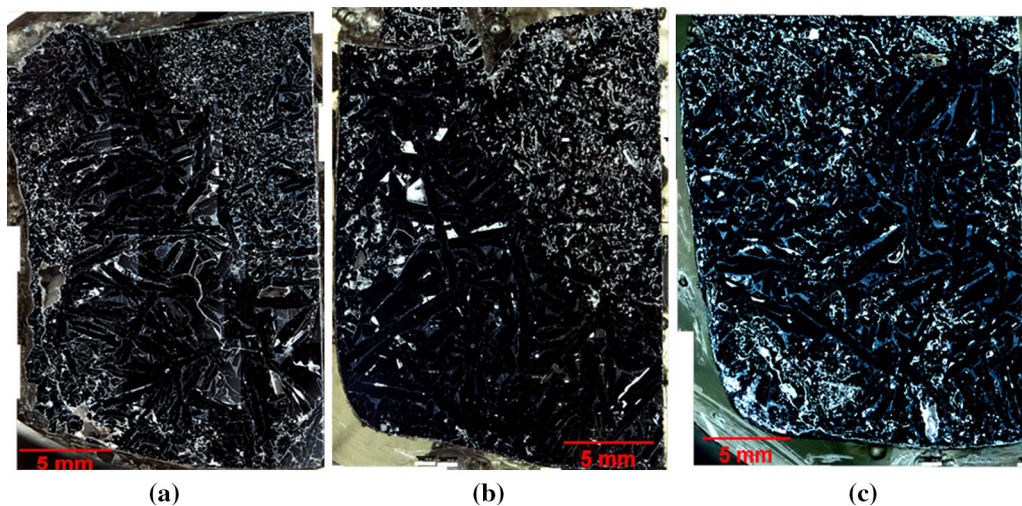


Fig. 19—Quarter cross-sectional macrographs showing the effect of separation time at coil current $I_{rms} = 278$ A and frequency $f = 65$ kHz for (a) 10 s, (b) 60 s, and (c) 120 s.

effect of joule heating associated with AC magnetic fields, higher currents result in greater power loss to joule heating and unwanted temperature rises, which may render the process inefficient. Makarav *et al.*^[23] analyzed conventional methods of EM separation comparing them based on their power efficiencies and concluded that an AC magnetic field is the most power inefficient. Figure 21 compares the effect of coil current on the separation process at a frequency of 65 kHz and separation time of 10 seconds. Significant improvements in the separation were observed when the coil current was increased from 278 to 330 A and to 533 A. At higher currents, there appears to be a deeper penetration of the settling forces, which draws the particles from the top central part and cements them at the bottom, resulting in a larger area of clean metal as shown in Figure 21(c). It can also be observed that particles close to the topmost part of the sample appear to be settling, an indication of a downward force acting on them.

Figure 22 compares the separation efficiency for various coil currents and the changes with time. The experimental data in the curves for $I_{rms} = 278$ and 330 A are exponential fits (see Eq. [5]), while the data

for $I_{rms} = 533$ A were predicted based on extrapolation of the values of λ for $I_{rms} = 278$ and 330 A. The points for 10 and 25 seconds on line $I_{rms} = 278$ A are from trial experiments using an *in situ* particle dispersion method in which clean metallurgical silicon was melted followed by the addition of Al-SiC composite and continuous stirring before the application of the EM field was made for particle separation.

E. Effect of Frequency

As seen in the fluid flow pattern, increasing the frequency enhances the fluid velocity, which is expected to improve the separation of particles especially due to particle settling, while the separation due to particle attachment to the side wall is limited as a result of skin-depth effect. Figures 23 and 24 compare the separation for 65, 75, and 90 kHz at a coil current of 278 A

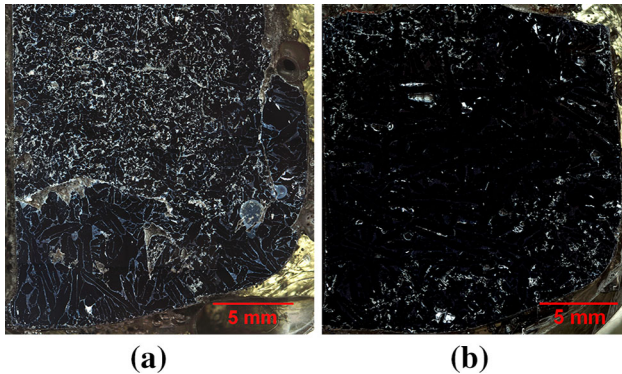


Fig. 20—Quarter cross-sectional macrographs showing the effect of separation time at coil current $I_{rms} = 278$ A and frequency $f = 90$ kHz for (a) 10 s, and (b) 60 s.

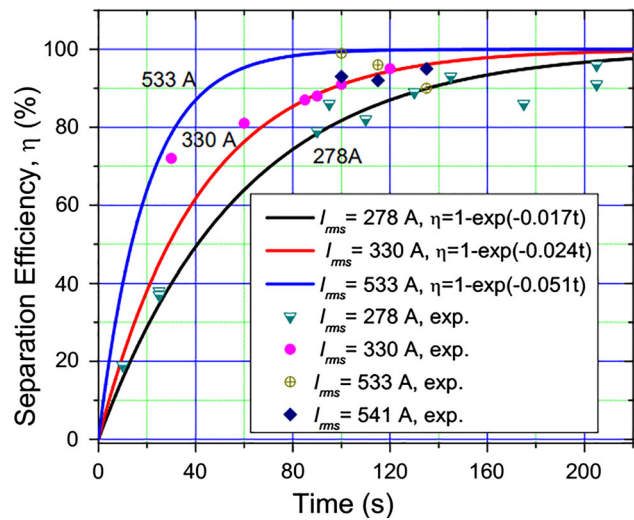


Fig. 22—The dependence of the separation efficiency on coil current and time at 65 kHz based on the corrected time for individual experiments.

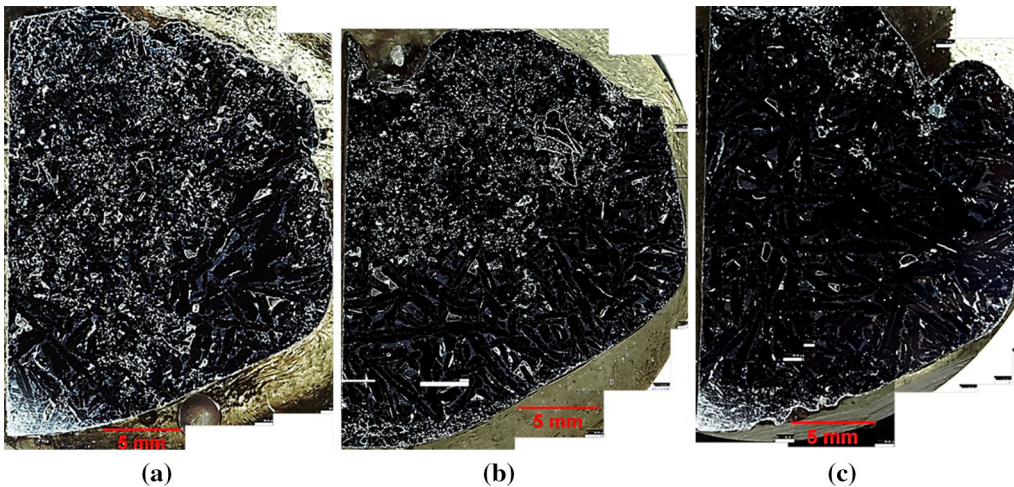


Fig. 21—Quarter cross-sectional macrographs comparing the effect of coil current (a) 278 A, (b) 330 A, (c) 533 A.

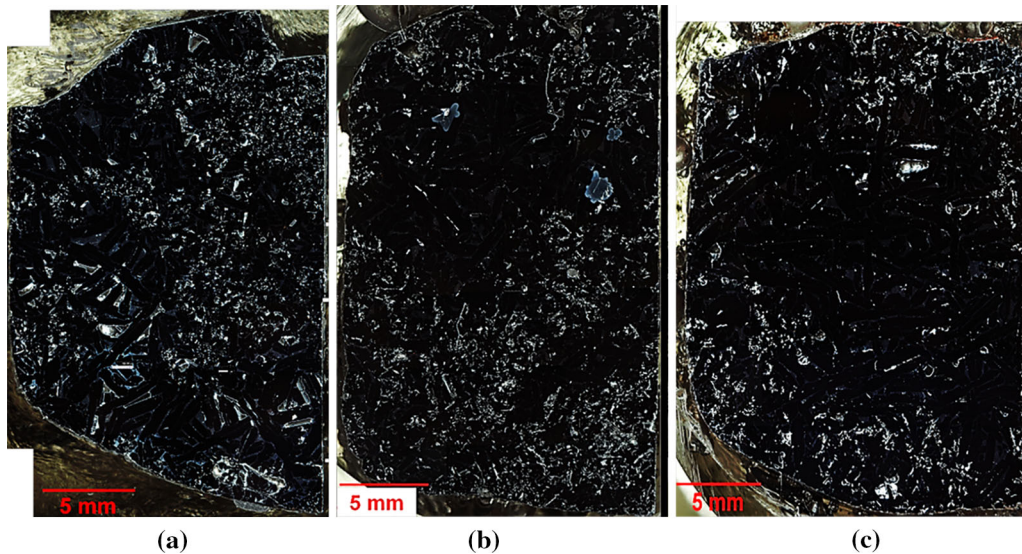


Fig. 23—Quarter cross-sectional macrographs showing the dependence of separation efficiency on frequency at 278 A and separation time of 45 s for (a) 65 kHz, (b) 75 kHz, and (c) 90 kHz.

for 45-seconds separation time. It can be seen that increasing the frequency significantly improved the separation by enhancing particle settling. Higher frequencies appear to have concentrated the settling force close to the top region to push the particles toward the bottom of the molten silicon. It is apparent from Eqs. [21] and [22] that higher frequencies result in stronger local fluid acceleration, and hence higher fluid shear force on the particles, leading to better settling.

Unlike the separation at 65 kHz, the clean matrix close to the side wall (left side) of the sample from top to the bottom was not observed for 75- and 90-kHz samples. Rather bulk settling of particles was observed, and the rate of settling is the highest for 90 kHz. It is worth mentioning that, the method to calculate the separation efficiency described in Section II–D could overestimate the separation for intermediate and even high frequencies due to the assumption that particles close to the bottom and side walls are deemed to have been effectively separated. However, for such frequencies, particles appear to be settling in the central part of the matrix which makes the calculation method less accurate. Therefore, the curve for 75 kHz reported in Figure 24 is an extrapolation based on those for 65 and 90 kHz.

Based on a preliminary study of this process, the result of which is reported elsewhere,^[19] the effect of frequency on the separation process was found to be related to the coil current. As shown in Figure 25, at low coil currents, higher frequency resulted in higher separation efficiencies, the difference of which is less pronounced at higher currents. At higher coil currents, the efficiency of the separation process depends more on the current than on the frequency.

IV. CONCLUSIONS

This study investigated the effect of EM field on the removal of nonmetallic inclusions from silicon. The

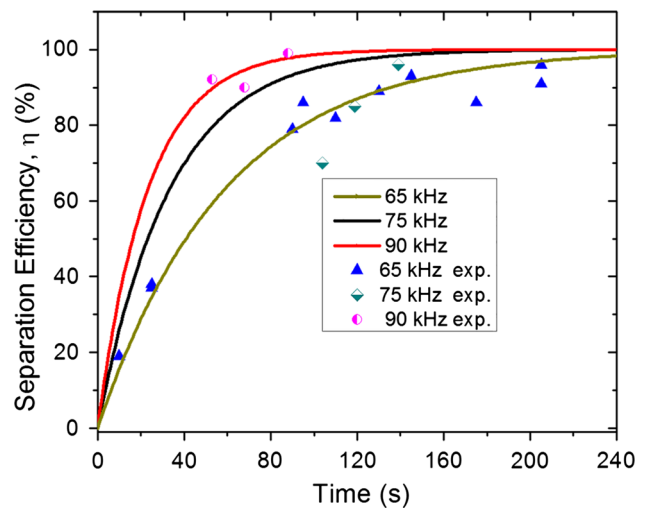


Fig. 24—The dependence of the separation efficiency on the frequency and separation time at a coil current of 278 A.

effects of particle size, separation time, frequency, and coil current on the separation process were evaluated. Inclusion-separation efficiencies of over 95 pct were recorded. The separation efficiency increased significantly with the increasing frequency, separation time, and coil current. Higher frequency induced stronger fluid flows, and higher coil currents resulted in stronger magnetic fields and induced fluid flows for enhanced particle separation. Longer separation times led to enhanced settling of the particles present at the top. Particles were separated from the matrix of the material and were trapped at the top, bottom, and side walls of the crucible. Three mechanisms accounted for the separation process:

1. Induced secondary fluid flow carried particles from the bulk of the melt, circulated them until either the

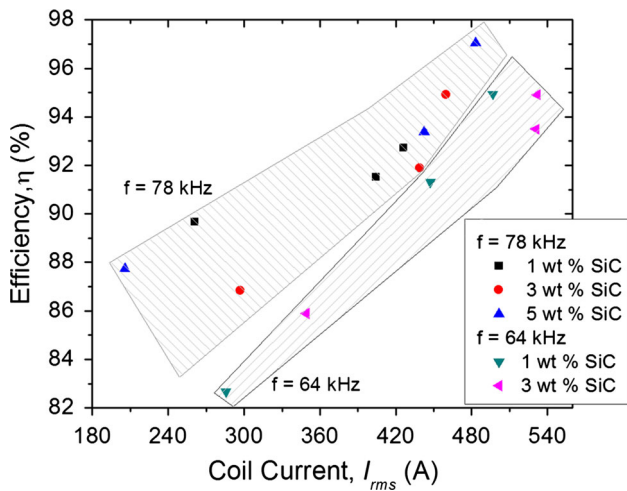


Fig. 25—Recorded separation efficiencies plotted against coil current for various frequencies and particle concentrations.

particles are acted upon by other physical forces (leading to trapping at the side wall or settling to the bottom) or they end up at the top central part of the molten silicon.

- Large inclusions were separated first to the side and bottom walls while small inclusions agglomerated and deposited at these sites due to the influence of the EM force on particles and fluid shear force.
- The contribution from the EM Archimedes force was to trap particles in the vicinity of the side wall of the crucible.
- Magnetic field and fluid flow simulation results showed uneven distribution of the magnetic field in the molten silicon, and the fluid had a circulatory flow pattern with the strongest flow at the bottom of the crucible, allowing particles in this region to settle fastest. Convective forces enhanced the effect of gravity forces to settle and held particles strongly to the bottom of the sample. Fluid shear force resulting from local fluid acceleration on the particles is believed to be the dominant force in the settling of the particles.

ACKNOWLEDGMENTS

This work was supported by the Department of Energy (Award No. DE-EE0000575), the Material

Research Center (MRC), and the Intelligent Systems Center (ISC) at Missouri University of Science and Technology (Missouri S&T). The contribution of Dr. Kent D. Peaslee at the Department of Materials Science and Engineering, Missouri S&T, who passed away in the course of this study, is greatly acknowledged. The authors are also grateful for support from the National Science Foundation China (Grant No. 51334002).

REFERENCES

- D. Sarti and R. Einhaus: *Sol. Energy Mater. Sol. Cells*, 2002, vol. 72 (1–4), pp. 27–40.
- N.B. Mason: *Proceedings of the Photovoltaic Science, Applications & Technology Conference*, Durham, 2007, pp. 43–46.
- A. Lotnyk, O. Breitenstein, and H. Blumtritt: *Sol. Energy Mater. Sol. Cells*, 2008, vol. 92, pp. 1236–40.
- L. Zhang, E. Øvrelid, S. Senanu, B. Agyei-Tuffour, and A.N. Femi: *Revas2008: 2008 Global Symposium on Recycling, Waste Treatment and Clean Technology*, TMS, Warrendale, PA, 2008, pp. 1011–26.
- O.S. Fishman: *Adv. Mater. Process.*, 2008, vol. 166 (10), pp. 33–34.
- O.S. Fishman: *Adv. Mater. Process.*, 2008, vol. 166 (9), pp. 39–40.
- G. Lavorel and M. LeBars: *Phys. Rev. E*, 2009, vol. 80, pp. 046324-1–4-8.
- L. Zhang and A. Ciftja: *Sol. Energy Mater. Sol. Cells*, 2008, vol. 92 (11), pp. 1450–61.
- A. Kolin: *Science*, 1953, vol. 117 (2), pp. 134–37.
- D. Leenov and A. Kolin: *J. Chem. Phys.*, 1954, vol. 22 (4), pp. 683–88.
- Y. Tanimoto and Y. Kakuda: *J. Phys. Conf. Ser.*, 2009, vol. 156, p. 012030.
- J.Y. Hwang, M. Takayasu, F.J. Friedlaender, and G. Kullerud: *J. Appl. Phys.*, 1984, vol. 55, pp. 2592–94.
- M. Motokawa: *Rep. Prog. Phys.*, 2004, vol. 67, pp. 1995–2052.
- Z. Sun, M. Guo, F. Verhaeghe, J. Vleugels, O. Van-der-Biest, and B. Blanpain: *Prog. Electromagn. Res. PIER*, 2010, vol. 103, pp. 1–16.
- K. Takahashi and S. Taniguchi: *ISIJ Int.*, 2003, vol. 43 (6), pp. 820–27.
- F. Yamao, K. Sassa, K. Iwai, and S. Asai: *Tetsu-to-Hagane*, 1997, vol. 83 (1), pp. 30–35.
- A. Dong, L. Zhang, and L.N.W. Damoah: *JOM*, 2011, vol. 63 (1), pp. 23–27.
- A. Dong, L. Damoah, and L. Zhang: *Supplemental Proceedings: Materials Processing and Energy Materials*, vol. I, TMS, Orlando, 2011, pp. 669–76.
- L.N.W. Damoah and L. Zhang: *EPD Congress 2012*, L. Zhang, A. Antoine and W. Cong, eds., The Minerals, Metals & Materials Society (TMS), Orlando, FL, 2012, pp. 501–08.
- L.-P. Wang and M.R. Maxey: *J. Fluid Mech.*, 1993, vol. 256, pp. 27–68.
- J. Ruiz, D. Macias, and F. Peters: *PNAS*, 2004, vol. 101 (51), pp. 17720–24.
- A. Aliseda, A. Cartellier, F. Hainaux, and J.C. Lasheras: *J. Fluid Mech.*, 2002, vol. 468, pp. 77–105.
- S. Makarov, R. Ludeig, and D. Apelian: *IEEE Trans. Magn.*, 2000, vol. 36 (4), pp. 2015–21.